ELSEVIER

Volume 183, Number 1, January 2010

JOURNAL OF SOLID STATE CHEMISTRY

www.elsevier.com/locate/jssc

CONTENTS

Abstracted/indexed in BioEngineering Abstracts, Chemical Abstracts, Coal Abstracts, Current Contents/Physics, Chemical, & Earth Sciences, Engineering Index, Research Alert, SCISEARCH, Science Abstracts, and Science Citation Index. Also covered in the abstract and citation database SCOPUS®. Full text available on ScienceDirect®.

Regular Articles

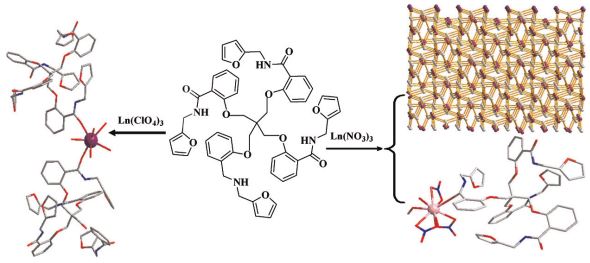

We present here a series of zero- to three-dimensional lanthanide coordination structures and luminescence properties of Eu(III) complex of a new tetrapodal ligand.

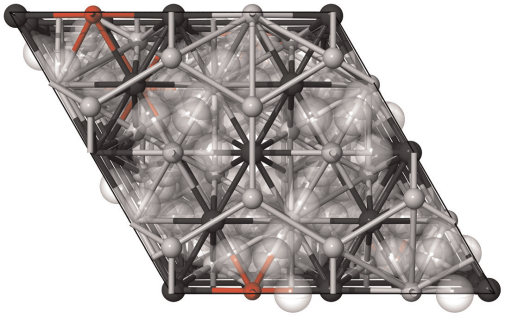

$CuLi_xMg_{2-x}$ with $x=0.08$ crystallizes in a $P6_222$ hexagonal structure in which Li (red) will substitute Mg1 (1/2, 0, z) sites (Mg-grey). Cu atoms are represented by black spheres and empty spaces by transparent ones.

Regular Articles—Continued

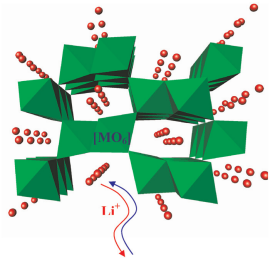

Ti-based ramsdellite compounds can make up cathode and anode materials for lithium batteries by introducing vanadium. Lithium deinsertion experiments on $LiTi_{2-y}V_yO_4$ materials develop a high operating voltage (3 V) useful as the cathode, while lithium insertion experiments yield a low operating voltage, 1.5 V, useful as the anode. Vanadium-rich compounds show specific theoretical capacity values in the high voltage range that are even comparable to those reported for $LiFePO_4$ which is presently one of the preferred cathode materials for lithium batteries.

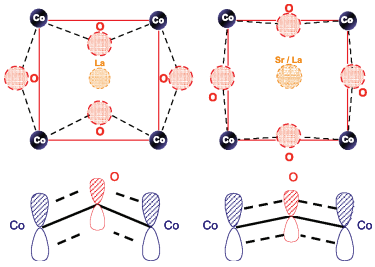

Change in spin multiplicity induced by the bigger size of Sr(II) cations, aligning the Co–O–Co atoms, and favoring the overlapping of π-symmetry cobalt and oxygen orbitals.

Continued

Magnetic properties of quadruple perovskites $Ba_4LnRu_3O_{12}$ (Ln = La, Nd, Sm–Gd, Dy–Lu)
Yuki Shimoda, Yoshihiro Doi, Makoto Wakeshima and Yukio Hinatsu
Page 33

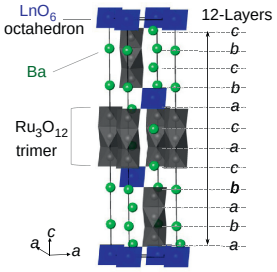

Quadruple perovskites $Ba_4LnRu_3O_{12}$ (Ln = La, Nd, Sm–Gd, Dy–Lu) were prepared. They adopt the 12L-perovskite-type structure consisting of Ru_3O_{12} trimers and LnO_6 octahedra. All of these compounds show an antiferromagnetic transition at 2.5–30 K. For $Ba_4NdRu_3O_{12}$, ferrimagnetic ordering has been observed at 11.5 K. The observed magnetic transition is due to the magnetic behavior of the $Ru_3^{4.33+}O_{12}$ trimer with $S=\frac{1}{2}$. Magnetic properties of $Ba_4LnRu_3O_{12}$ were compared with those of triple perovskites $Ba_3LnRu_2O_9$ and double perovskites Ba_2LnRuO_6.

Order–disorder transition in the $Nd_{2-y}Y_yZr_2O_7$ system: Probed by X-ray diffraction and Raman spectroscopy
B.P. Mandal, P.S.R. Krishna and A.K. Tyagi
Page 41

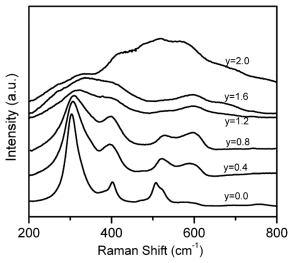

In $Nd_{2-y}Y_yZr_2O_7$ series, the structure changes from pyrochlore to defect fluorite with increase in Y content in the series. The Raman spectra explicitly shows how the structural changes take place in the system.

Ab-initio study of the structural, linear and nonlinear optical properties of $CdAl_2Se_4$ defect-chalcopyrite
T. Ouahrani, Ali H. Reshak, R. Khenata, B. Amrani, M. Mebrouki, A. Otero-de-la-Roza and V. Luaña
Page 46

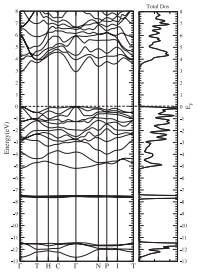

Calculated band structure and total density of $CdAl_2Se_4$.

Thermolysis of lanthanide dithiocarbamate complexes
William L. Boncher, Michelle D. Regulacio and Sarah L. Stoll
Page 52

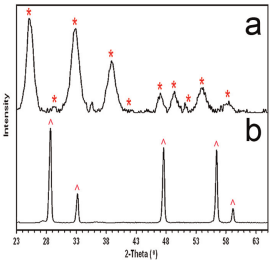

Polycrystalline lanthanide sulfide materials were formed at low temperatures using a single-source precursor based on the lanthanide dithiocarbamate complex.

TiO_2 nanotube, nanowire, and rhomboid-shaped particle thin films fixed on a titanium metal plate
Yuko Inoue, Iwao Noda, Toshio Torikai, Takanori Watari, Takao Hotokebuchi and Mitsunori Yada
Page 57

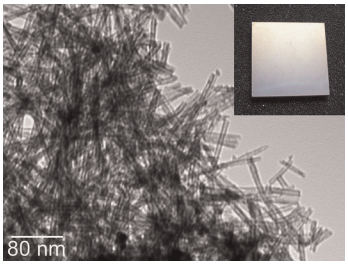

Titanium dioxide nanotube, nanowire, and rhombic particle thin films could be formed by various treatments on a sodium titanate nanotube thin film fixed on a titanium metal plate.

$Sn_x[BPO_4]_{1-x}$ composites as negative electrodes for lithium ion cells: Comparison with amorphous $SnB_{0.6}P_{0.4}O_{2.9}$ and effect of composition
Donato Ercole Conte, Abdelmaula Aboulaich, Florent Robert, Josette Olivier-Fourcade, Jean-Claude Jumas, Christian Jordy and Patrick Willmann
Page 65

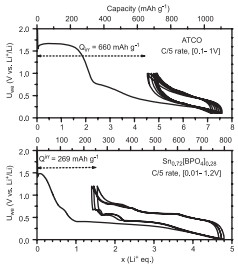

Galvanostatic discharge-charge curves of ATCO and $Sn_{0.72}[BPO_4]_{0.28}$ composite materials at C/5 rate, respectively.

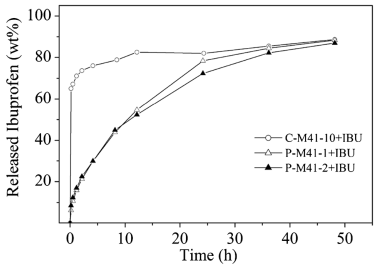

The distribution of DMS groups on the pore surfaces of the mesostructures strongly affects the drug release rate. The P-M41-1 and the P-M41-2 possess the close DMS modification levels as the C-M41-10, but the ibuprofen release rates from the P-M41-1 and P-M41-2 are much slower than that from the C-M41-10.

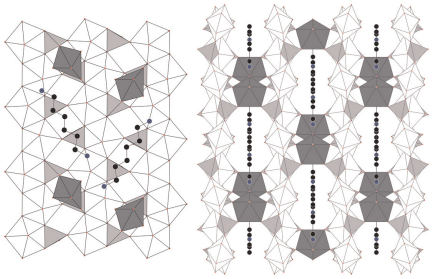

The $(C_6N_2H_{20})\{[(UO_2)(H_2O)][(UO_2)(VO_4)]_4\}$ compound: projection in the (1 0 0) and in the (0 0 1) planes showing the amine position.

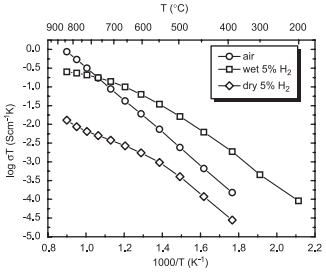

Potassium doped barium zirconates have been synthesized by solid state reactions. It was found that the solubility limit of potassium on *A*-sites is between 5% and 10 %. The sintering conditions and conductivity can be improved significantly by adding 1 wt% ZnO during material synthesis. Five percent doping of potassium at *A*-site can double the total conductivity.

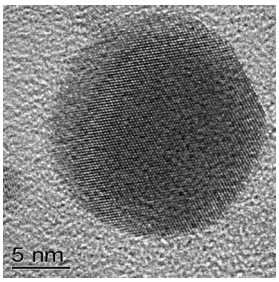

Biopolymer chitosan was used as stabilization media to synthesize both magnetite and magnetite/silver core/shell nanoparticles. Results of HRTEM and NBD patterns confirm core/shell morphology of the obtained nanoparticles. It was found that the composites show diluted magnet-like behavior.

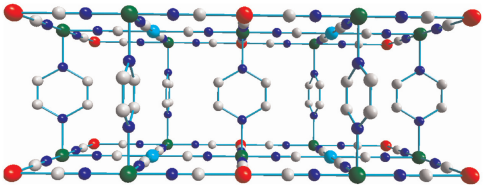

Low temperature ordered structure for pyrazine in $T[Ni(CN)_4]\cdot$ pyz.

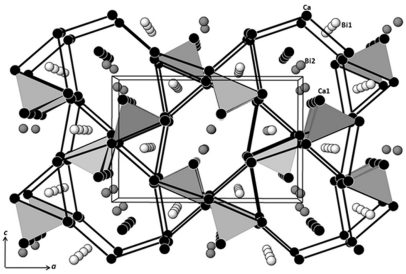

The structure of $Ca_5Bi_3H_{0.93}$ occurs in the novel Ca_5Sb_3F structure type with D centered in the shaded calcium tetrahedra.

Continued

MAS-NMR studies of lithium aluminum silicate (LAS) glasses and glass–ceramics having different Li_2O/Al_2O_3 ratio

A. Ananthanarayanan, G.P. Kothiyal, L. Montagne and B. Revel

Page 120

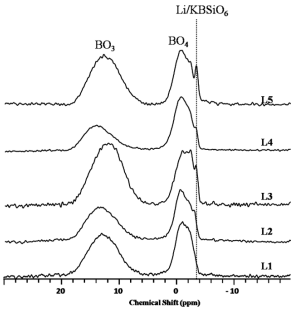

The ^{11}B MAS-NMR spectra of lithium aluminum silicate (LAS) glass–ceramics indicating the formation of $Li/KBSiO_6$ phase. This phase is isostructural with virgilite and cannot be distinguished in X-ray diffractograms.

Crystallization of niobium germanosilicate glasses

Rodrigo Santos, Luís F. Santos, Rui M. Almeida, Joachim Deubener and Lothar Wondraczek

Page 128

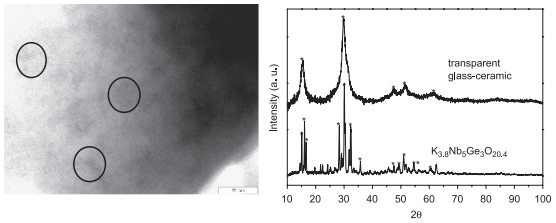

TEM image and XRD pattern of the glass ceramic produced (circles indicate nanocrystals).

First-principle studies of Ca–*X* (*X* = Si,Ge,Sn,Pb) intermetallic compounds

Zhiwen Yang, Dongmin Shi, Bin Wen, Roderick Melnik, Shan Yao and Tingju Li

Page 136

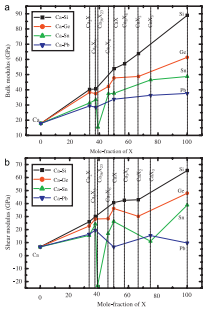

Calculated (a) bulk moduli and (b) shear moduli of Ca–*X* system intermetallic compounds.

Carbon nanotube—chalcogenide glass composite

Stepan Stehlik, Jiri Orava, Tomas Kohoutek, Tomas Wagner, Miloslav Frumar, Vitezslav Zima, Toru Hara, Yoshio Matsui, Kazuyuki Ueda and Martin Pumera

Page 144

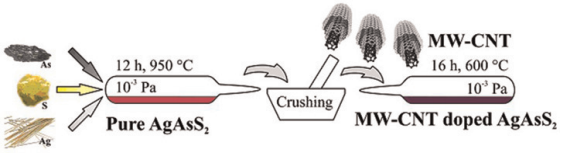

Preparation of multi-walled carbon nanotube-doped chalcogenide glasses by direct synthesis and the melt-quenching method

---

Sandwich-type polyoxotungstate hybrids decorated by nickel-aromatic amine complexes

Peng-Tao Ma, Jun-Wei Zhao, Jing-Ping Wang, Yue Shen and Jing-Yang Niu

Page 150

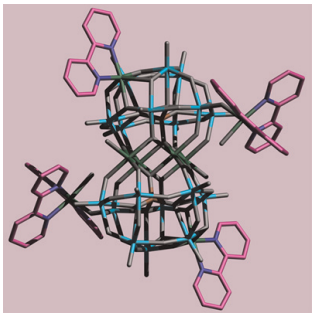

Three new sandwich-type polyoxotungstates (POTs) decorated by nickel-2,2'-bpy complexes were successfully synthesized under hydrothermal conditions and structurally characterized.

(Ca/Sr)Au_xCd_{1-x}: Stacking variants of the CrB–FeB series

Wiebke Harms, Ines Dürr, Michael Daub and Caroline Röhr

Page 157

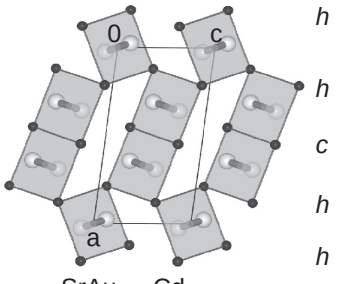

$SrAu_{0.93}Cd_{0.07}$

$SrAu_{0.93}Cd_{0.97}$, one of the stacking sequences of the CrB/FeB structure type series found in the quasibinary section SrAu–SrCd.

Antiferromagnetism of perovskite $EuZrO_3$
Yanhua Zong, Koji Fujita, Hirofumi Akamatsu, Shunsuke Murai and Katsuhisa Tanaka
Page 168

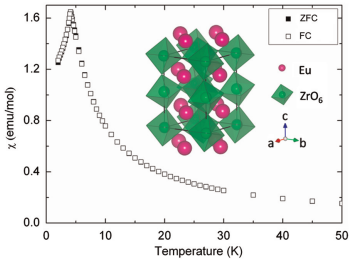

Perovskite $EuZrO_3$ with almost all Eu ions present as Eu^{2+} has been synthesized and its structure and magnetic properties have been studied. An antiferromagnetic transition was observed around 4.1 K for the first time. The mechanism of the magnetic transition has been discussed.

Crystal structures of three intermetallic phases in the Mo–Pt–Si system
J.-M. Joubert, Ya. Tokaychuk and R. Černý
Page 173

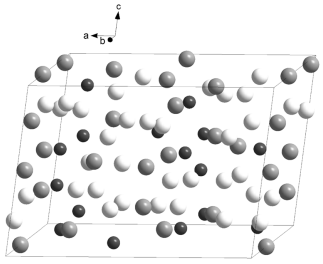

The crystal structures of three ternary Mo–Pt–Si intermetallic compounds have been determined *ab initio* from powder X-ray diffraction data. The three structures represent new structure types.

Neutron powder diffraction study of tetragonal $Li_7La_3Hf_2O_{12}$ with the garnet-related type structure
Junji Awaka, Norihito Kijima, Kunimitsu Kataoka, Hiroshi Hayakawa, Ken-ichi Ohshima and Junji Akimoto
Page 180

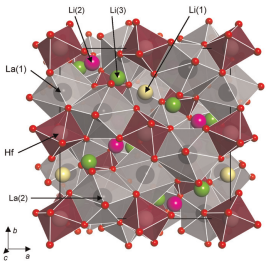

The crystal structure of tetragonal $Li_7La_3Hf_2O_{12}$ had the garnet-related type structure with a space group of $I4_1/acd$ (no. 142) with the lattice constants of $a = 13.106(2)$ Å and $c = 12.630(2)$ Å. The tetragonal $Li_7La_3Hf_2O_{12}$ had the fully ordered Li arrangement.

Crystal structure of the monoclinic and cubic polymorphs of $BiMn_7O_{12}$
H. Okamoto, N. Imamura, M. Karppinen, H. Yamauchi and H. Fjellvåg
Page 186

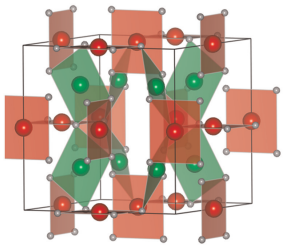

The complex perovskite $BiMn_7O_{12}$ occurs with polymorphic structures, cubic and monoclinic. Structural analysis reveals unusual behavior for oxygen and bismuth in the monoclinic and cubic phases, respectively. Unusually large (and anisiotropic) displacement parameters for some of the oxygen ions in the monoclinic phase indicated competition between non-equivalent Mn–O bonds for the corner-sharing *d*-type JT Mn_BO_6 and square-planar $Mn_{A''}O_4$ polyhedra.

Photocatalytic splitting of water under visible-light irradiation over the NiO*x*-loaded Sm_2InTaO_7 with $4f$-d^{10}-d^0 configuration
Xinde Tang, Hongqi Ye, Hui Liu, Chenxia Ma and Zhi Zhao
Page 192

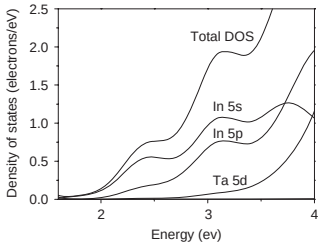

A new visible-light-response photocatalyst Sm_2InTaO_7 with $4f$-d^{10}-d^0 configuration was developed. DFT calculation indicated that strong dispersion from the hybridized In 5*s* 5*p* orbitals was responsible for the high photocatalytic activity.

Comparative study of the synthesis of layered transition metal molybdates
S. Mitchell, A. Gómez-Avilés, C. Gardner and W. Jones
Page 198

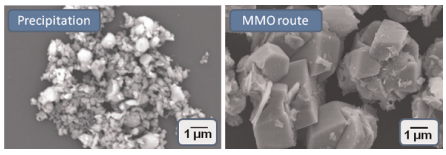

Mixed metal oxides (MMOs) derived from layered double hydroxide precursors differ in their reactivity on exposure to aqueous molybdate containing solutions. We investigate the influence of the molybdate source, the rehydration pH and the ratio of *T*/Mo on the reactivity of some *T*–Al containing MMOs (*T* = Co, Ni, Cu or Zn) towards the formation of layered transition metal molybdates of general formula $AT_2(OH)(MoO_4)_2 \cdot H_2O$ (where $A^+ = NH_4^+$, K^+ or Na^+).

Continued

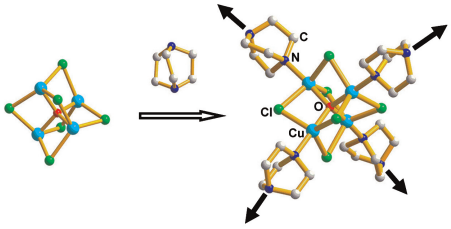

The metal-organic framework $[Cu_4OCl_6(DABCO)_2] \cdot 0.5DABCO \cdot 4CH_3OH$ (**MFU-5**) is constructed from a molecular precursor containing $\{Cu_4OCl_6\}$ secondary building units which become cross-linked into a 3D zeolite-type network with hexagonal symmetry by linear DABCO ligands (DABCO = 1,4-diazabicyclo[2.2.2]octane).

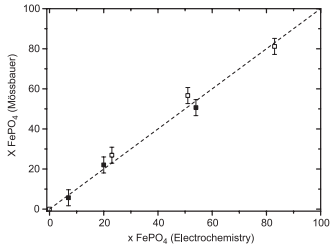

Relative amount of $FePO_4$ obtained by Mössbauer and electrochemical data. We have corrected Mössbauer spectral intensities with our *f* factor of both $LiFePO_4$ and $FePO_4$. Open (filled) squares correspond to values obtained during charging (discharging) process. The dashed line, given as a guideline for the eye, corresponds to the ideal case were amounts deduced from different experimental measurements are equal.

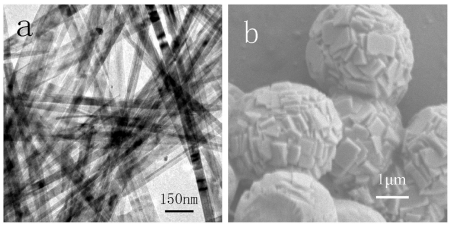

Hexagonal NiS nanobelts and cubic NiS_2 microspheres were hydrothermally synthesized in the reaction of $Ni(CH_3COO)_2 \cdot 4H_2O$ and $Na_2S_2O_3 \cdot 5H_2O$.

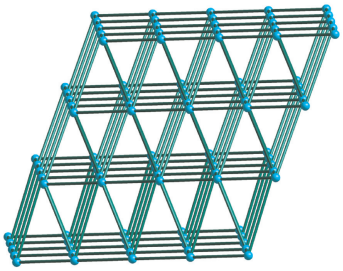

Compound **1** is the POM-based unprecedented eight-connected self-penetrating organic–inorganic hybrid network constructed from the cuprous chloride clusters $[Cu_6Cl_3]$, Lindquist-type polyoxoanions $[Mo^VW_5O_{19}]$, and the 4,4′-bipyridine ligands.

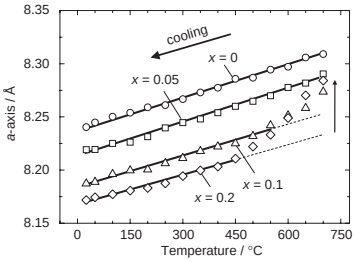

Non-linear variation of lattice parameters of the Li excess $LiMn_2O_4$ spinels was observed during cooling process from 700 to 25 °C.

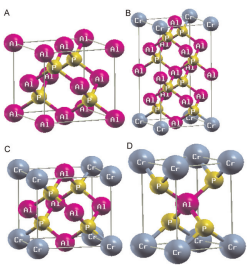

The prototype structures of Cr doped AlX (X = N, P, As, Sb) compounds: (A) zinc blende AlP for x=0, (B) $Cr_1Al_7P_8$ for x = 0.125, (C) $Cr_1Al_3P_4$ for x = 0.25, (D) $Cr_1Al_1P_2$ for x = 0.5.

Neutron diffraction study of phase transitions in perovskite-type strontium molybdate $SrMoO_3$
René B. Macquart, Brendan J. Kennedy and Maxim Avdeev
Page 250

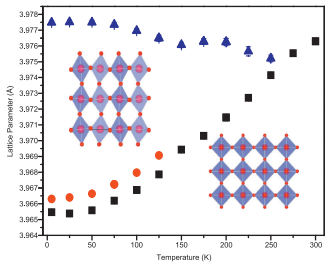

Variable temperature neutron diffraction measurements of $SrMoO_3$ from 5 K to room temperature show the presence of two phase transitions associated with tilting of the octahedra. On cooling, the structure transforms from cubic ($Pm\bar{3}m$) to tetragonal ($I4/mcm$) and ultimately orthorhombic ($Imma$).

High pressure synthesis and properties of ternary titanium (III) fluorides in the system $KF–TiF_3$ containing regular pentagonal bipyramids $[TiF_7]$
Shoji Yamanaka, Akira Yasuda and Hajime Miyata
Page 256

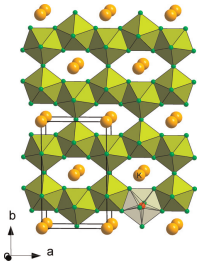

A new ternary fluoride KTi_2F_7 has been developed under high-pressure and high-temperature conditions, which contains pentagonal bipyramid polyhedra $[TiF_7]$.

The influence of sulfur substitution on the atomic displacement in $Bi_2Ti_2O_7$
Beverly Brooks Hinojosa, Paul M. Lang and Aravind Asthagiri
Page 262

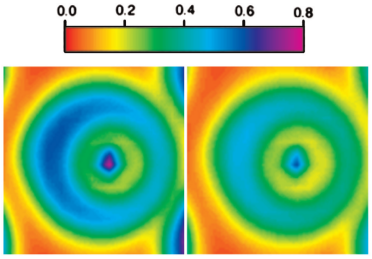

The electron localization function for $Bi_2Ti_2O_6O'$ and $Bi_2Ti_2O_6S'$ respectively show that sulfur substitution on the O′ site will suppress lone pair formation.

Homochiral frameworks derived from magnesium, zinc and copper salts of L-tartaric acid
Jeffrey A. Rood, Bruce C. Noll and Kenneth W. Henderson
Page 270

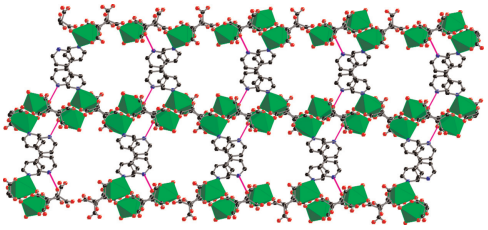

Five metal-organic frameworks derived from L-tartarate and the divalent metal ions magnesium, zinc or copper have been prepared and structurally characterized. Significant structural diversity is displayed within this set of complexes.